Research Square

Preprints are preliminary reports that have not undergone peer review.
They should not be considered conclusive, used to inform clinical practice,
or referenced by the media as validated information.

Enhancing Dielectric Breakdown Strength in $BiFeO_3$-$SrTiO_3$ Ceramics via $Bi_2Ti_2O_7$ Doping

Chang Sheng
Jilin University
Xiaoming Qiu
Jilin University
Haoyu Tang
Jilin University
Wenwei Ge
wenweige@jlu.edu.cn
Jilin University https://orcid.org/0000-0001-7845-2267
Jingwei Liang
Jilin University
Changyi Liu
Jilin University
Hongwei Zhao
Jilin University
Haiyan Yu
ChangChun SanYou Automobile Parts Manufacture Co..Ltd

Research Article

Keywords: $BiFeO_3$-SrTiO3, $Bi_2Ti_2O_7$, Energy storage, Dielectric breakdown strength, Ferroelectric

Posted Date: November 10th, 2026

DOI: https://doi.org/10.21203/rs.3.rs-11659673/v1

License: This work is licensed under a Creative Commons Attribution 4.0 International License.
Read Full License

Additional Declarations: The authors declare no competing interests.

Enhancing Dielectric Breakdown Strength in $BiFeO_3$-$SrTiO_3$ Ceramics via $Bi_2Ti_2O_7$ Doping

Chang Sheng[1], Xiaoming Qiu[1], Haoyu Tang[1], Wenwei Ge[1, *], Jingwei Liang[1], Changyi Liu[2], Hongwei Zhao[3], and Haiyan Yu[4]

[1]*Key Laboratory of Automobile Materials of Ministry of Education, School of Materials Science and Engineering, Jilin University, Changchun, Jilin 130022, China*

[2]*Key Laboratory of Bionic Engineering Ministry of Education, Jilin University, Changchun, Jilin 130025, China*

[3]*School of Mechanical and Aerospace Engineering, Jilin University, Changchun, Jilin 130025, China*

[4]*ChangChun SanYou Automobile Parts Manufacture Co..Ltd, Changchun, Jilin 130103, China*

Abstract:

(1-*x*)(0.7$BiFeO_3$-0.3$SrTiO_3$)-*x*$Bi_2Ti_2O_7$ ceramics (abbreviated as BFST-*x*BTO, where x = 0, 0.02, 0.04, 0.06, and 0.08) were synthesized via a solid-state reaction method. The BFST and BTO ceramic powders were separately prepared using the solid-state reaction approach. Subsequently, these two types of powders were homogeneously mixed to fabricate BFST-*x*BTO solid solution ceramics. X-ray diffraction (XRD) analysis confirms that BTO diffuses into the crystal lattice of BFST, forming perovskite solid solution ceramics. With the increase of BTO content, the average grain size of the ceramics decreases, while the band gap shows a corresponding increasing trend. Impedance analysis indicates that the conduction mechanism of the ceramics is dominated by oxygen vacancy hopping near the grain boundaries. Notably, the introduction of BTO leads to increased grain boundary density and an expanded band gap, which jointly contribute to the reduced dielectric loss and enhanced dielectric breakdown strength (E_b) of the ceramics. The E_b, recoverable energy storage density (W_{rec}) and efficiency (η) for BFST without BTO doping are 140 kV/cm, 0.38 J/cm^3 and 10.67%. After BTO-doping, E_b, W_{rec} and η are all increased. The highest E_b=420 kV/cm

is obtained in BFST-0.04BTO ceramics. The W_{rec} and η are 2.24 J/cm^3 and 34.74% for BFST-0.04BTO ceramics. With increasing BTO content to 0.08, The E_b slightly decreases to 400 kV/cm, while the W_{rec} and η increase to 3.38 J/cm^3 and 39.88%, respectively.

Keywords: $BiFeO_3$-$SrTiO_3$; $Bi_2Ti_2O_7$; Energy storage; Dielectric breakdown strength; Ferroelectric

*Author to whom correspondence should be addressed. Electronic mail: wenweige@jlu.edu.cn

1 Introduction

The shift to clean energy and environmental protection are the defining challenges of our era. The extensive extraction and burning of fossil fuels lead to environmental pollution and global warming[1]. The intermittent nature of renewable clean energy necessitates advanced energy storage technology. In recent years, designing energy storage materials with high energy storage density, low energy loss and low environmental burden[2, 3] become a hot issue that researchers pay attention to. Dielectric ceramic capacitors have the advantages of high power density, wide temperature range, fast charge and discharge speed and long service cycle[4]. However, their low energy storage density limits its applications in energy storage[5]. To improve energy storage density, many efforts have been directed towards lead-based materials, which provide higher storage densities than other dielectric materials[6]. However, a major drawback is that the high content lead-based materials can severely pollute the environment and serious risks to human health[7]. In response to the growing demand for sustainable development, many countries and regions have enacted laws and regulations to prohibit or restrict the use of toxic metals such as lead, chromium (Cr), and mercury (Hg)[8]. Thus, in the past few years, the energy storage performance of lead-free perovskite ceramics has been extensively investigated and made remarkable progress.

The energy storage density (W), recoverable energy storage density (W_{rec}), and efficiency (η) can be calculated using the following Eqns. (1)-(3), based on the measured polarization-electric field (P-E) hysteresis loops:

$$W = \int_0^{P_{max}} E\mathrm{d}P \tag{1}$$

$$W_{rec} = \int_{P_r}^{P_{max}} E\mathrm{d}P \tag{2}$$

$$\eta = \frac{W_{rec}}{W} \mathrm{x}100\% \tag{3}$$

where P_{max} represents the polarization of a dielectric material under its dielectric breakdown strength (E_b) and P_r is remanent polarization after removing the E-field. Dielectric energy storage ceramics are classified into five categories: linear dielectrics

(LD), ferroelectrics (FE), relaxor ferroelectrics (RFE), antiferroelectrics (AFE), and relaxor-antiferroelectrics (RAFE)[9, 10]. FE ceramics possess high P_{max} and, but they also suffer from high P_r and significant hysteresis [11], which leads to low efficiency (η).Thus, reducing hysteresis by doping with linear dielectrics presents a promising strategy for enhancing their energy storage performance (ESP).

Among all the ABO_3 perovskite type FE materials, $BiFeO_3$ (BFO) exhibits high spontaneous polarization (P_s, approximately 90 μC/cm²) and a high Curie temperature ($T_c \approx 830°C$). Thus, BFO is considered one of the most promising base materials for designing high-performance energy storage dielectrics. However, pure BFO suffers from issues such as high leakage current, which significantly limits its breakdown strength (E_b). As a result, the maximum polarization (P_{max}) remains considerably lower than the saturation polarization (Ps) [12-15], thereby adversely affecting the energy storage performance-particularly in terms of energy storage density and breakdown strength.[16, 17]. $SrTiO_3$(STO) also adopts a perovskite structure and show linear dielectrics properties at room temperature, featuring high dielectric constant, low dielectric loss, and temperature- and frequency-insensitive dielectric properties[18, 19]. BFO and STO can form solid solutions (BFST) exhibiting an enhanced temperature stability of dielectric constant and E_b [20-24]. However, its E_b and W remain relatively low, which are the issues requiring attention at present [4, 25, 26].

$Bi_2Ti_2O_7$ (BTO) often appears in Bi-based perovskite ceramics as a secondary phase when the sintering condition is not well controlled. It is a typical LD material with extra high E_b and low hysteresis. Notably, several studies have demonstrated that the presence of the BTO phase in ceramics is conducive to enhancing energy storage performance. Wu et al. discovered the presence of BTO as a secondary phase in their study of BFBT-*x*NN, which was found to contribute to an improvement in the E_b [27]. Zhao et al. demonstrated through phase-field simulations that the presence of a certain amount of BTO phase with low ε_r enhances the ability to withstand higher loading voltages, thereby reducing the required loading voltage for the perovskite main phase[28]. However, in these previous studies, the BTO phase was formed as an uncontrolled by-

product without accurate regulation. The BTO phase generally exists as a secondary phase in ceramic systems. Most available modification strategies rely on external dopants to improve the ceramic performance, while studies on ceramic modification without introducing foreign phases remain scarce. From the perspective of chemical composition, all constituent elements of the BTO phase (Bi, Ti, O) are also the primary components of the BFST matrix. Bismuth volatilization takes place during the fabrication of BFST ceramics, and the introduction of BTO can compensate for the vacancy defects induced by such volatilization[29]. To clarify the underlying mechanism of energy storage performance (ESP) enhancement, BFST and BTO ceramic powders were first synthesized separately, followed by mixing, ball milling, and sintering. Since all elements in BTO are also components of the BFST matrix, this preparation process is analogous to the reactive template grain growth (RTGG) method [30]. After sintering, BTO diffuses into the lattice of BFST ceramics, leading to a significant enhancement in breakdown strength (E_b). Therefore, exploring the influence of BTO introduction routes on the energy-storage performance of BFST ceramics can provide experimental and theoretical guidance for optimizing the energy-storage properties of Bi-based perovskites.

2 Experimental Section

2.1 Materials Synthesis

$Bi_2Ti_2O_7$ (BTO) and $0.7BiFeO_3$-$0.3SiTiO_3$ (BFST) ceramic powders were first synthesized separately via solid state reaction method, and all sintering processes were performed in air. For BTO preparation, reagent grade raw materials of $NaBiO_3$•$2H_2O$ (≥99%) and TiO_2 (≥98%) were accurately weighed and dried at 120 ℃ for 2 h. Then, the raw materials were mixed in a ball mill for 1 h at a rotating speed of 150 rpm. Filter and precipitate the milling powder for 24 hours. After drying, the mixed raw materials were calcined at 900 ℃ for 3 h to obtain the BTO powders. The reagent grade raw materials of Fe_2O_3 (≥99%), TiO_2 (≥99%), Bi_2O_3 (≥99%) and $SrCO_3$ (≥99%) were used to fabricate BFST ceramic powders. The experimental procedure was the same as that of BTO. The distinction is that the calcine condition of the BFST ceramics was 800 ℃

for 3 h. The synthesized BFST and BTO ceramic powders were mixed according to the mole ratio of (1-*x*)BFST-*x*BTO (*x* = 0, 0.02, 0.04, 0.06, 0.08). The mixed powders were calcined at 800 ℃ for 3 h. The calcined powders were ball-milled again in a planetary ball mill for 8 h at a rotating speed of 300 rpm. After ball-milling, the mixtures were dried and pressed into discs with a diameter of 10mm under a cold isostatic pressure. Finally, the discs were sintered at 1000 ℃ for 2 h to obtain the (1-*x*)BFST-*x*BTO ceramics.

2.2 Characterization

The crystal structure of the ceramics was characterized by X-ray diffraction meter (D/max-2500PC) at room temperature. The microstructure and grain size of the ceramics were observed by scanning electron microscope (SEM) equipped with an energy dispersive spectrometer (EDS). The SEM samples were thermally etched. Specifically, they were heated at a rate of 5 °C/min to 950 °C and held at this temperature for 30 minutes. The dielectric properties of ceramics were analyzed by dielectric temperature spectrometer (DMS-500). The ferroelectric properties and energy storage properties of ceramics were tested by ferroelectric tester (Precision LC II). For dielectric measurements, both sides of the sample were silver-plated with electrodes. The silver electrodes were dried at 600 ˚C for 0.5 h. In the ferroelectric test, the sample thickness is about 0.15mm and gold electrodes with a diameter of 2 mm were sputtered. The UV–vis absorption spectra were collected by using an UV-VIS-NIR spectrophotometer (SHIMADZU, UV-3600Plus, Japan). X-ray photoelectron spectra (XPS) were conducted by using an ESCALAB 250Xi spectrometer and all data were fitted by Gaussian-Lorentzian function using XPSpeak41 software. The impedance spectra were obtained by measuring the polished ceramics pasted with silver electrodes using an LCR meter (HIOKI, IM3536, Japan) in the frequency range of 10 Hz to 2 MHz and all data were fitted by ZView software.

3 Results and discussion

Fig. 1(a) exhibits the XRD patterns of BTO and BFST-*x*BTO ceramics. According to the PDF card #32-0118, all peaks belong to BTO phase, which confirmed that BTO

was successfully synthesized without any secondary phase. All BFST-*x*BTO ceramics exhibit pure perovskite structure without any observable impurity phases. These results indicate that BFST and BTO can form a complete solid solution. Figs. 1(b)-(d) show the magnified diffraction peaks of perovskite cubic (110), (111), and (200). BTO doping modifies the crystal structure of BFST, as evidenced by the vanishing of peak splitting.

In order to better analyze the structure change of BFST-*x*BTO ceramics, the GSAS&EXPGUI software was used to refine the XRD data, as shown in Figs. 2(a)-(e). The refinement results confirm that the crystal structure of BFST-xBTO is *R3c* symmetry. The R_{wp} and χ^2 values are within acceptable ranges, verifying the reliability of the Rietveld refinement. As shown in Fig. 2(f), after the incorporation of BTO, the lattice parameter a_h increased while c_h decreased. The combined effect of these changes is that the unit cell volume increases following BTO doping. Atomic positional configurations dictate the magnitude of lattice distortion, which in turn modulates the dynamic behavior of electric dipoles, thereby shaping the profile of the ferroelectric hysteresis loop[31, 32]. Table 1 summarizes the variations in the atomic positional parameters of the BFST-*x*BTO ceramic. As manifested in the table, the B-site atoms undergo a centripetal displacement, and the maximum centripetal shift of B-site atoms is attained at x = 0.04. Accordingly, it can be deduced that the incorporation of BTO propels the B-site atoms to migrate toward the center of the oxygen octahedron, which reduces the ferroelectric ordering degree and ultimately facilitates the optimization of the energy storage performance of the ceramics.

Figure 3 displays the SEM micrograph of the BFST-*x*BTO ceramics after thermal etching. All the ceramics exhibit a dense and homogeneous microstructure. The grain size distribution diagrams for BFST-*x*BTO ceramics are shown as insets of Figure 3(a)-(e). The corresponding fitting curves were obtained by distribution fitting based on raw grain size data, from which the average grain size was extracted. With the addition of BTO, the grain size becomes more uniform, and the average grain size (AGS) first decreases and then slightly increases, reaching its minimum at 4 mol% BTO, with a value of 0.84 μm. (see Fig. 3(f)). The grain size of the ceramics is mainly determined

by the sintering temperature, the initial powder particle size, the additives, etc[33]. For the BFST-*x*BTO ceramics, both the sintering profile and the precursor powder size were held constant, variations in average grain size can be primarily attributed to the content of the addition of BTO. As the grain size decreases, the grain boundary density increases, thereby reducing the mobility of charge carriers. Furthermore, grain refinement homogenizes the internal electric field distribution, thereby enhancing the overall structural and electrical stability of the ceramics and ultimately contributing to the improved dielectric breakdown strength. [34-36]. Therefore, BTO doping contributes positively to the E_b of BFST-xBTO ceramics.

Fig. 4(a)-(f) presents the SEM micrographs and their corresponding EDS mapping images of BFST-0.04BTO ceramics. Every constituent element is homogeneously dispersed across the ceramic, with no evidence of local enrichment. This observation confirms that BTO has successfully incorporated into the BFST ceramics, which is consistent with the result obtained from XRD.

Figures 5(a)-5(e) display the temperature dependent dielectric constant (ε_r) and loss tangent (tanδ) of BFST-*x*BTO ceramics at 1 kHz - 1 MHz. An obvious frequency dispersion can be seen from room temperature to 200°C, which indicates the characteristic of relaxor ferroelectric due to the existence of polar nanoregions (PNRs) [37-39]. Above 200°C, enhanced ε_r and tanδ under low frequencies are caused by the leakage conductivity. Fig. 5(f) presents the ε_r-T (solid lines) and tanδ-T (dash lines) curves at l MHz. Obviously, with BTO doping, the leakage enhanced ε_r and tanδ above 350 °C is suppressed and enhanced temperature stability of ε_r and tanδ are obtained. A lower tanδ value facilitates the suppression of leakage current, which endows the samples with a higher E_b[40].

Fig. 6(a)-(d) presents the P-E curves of the BFST-*x*BTO ceramics under different electric fields before breakdown. The W_{rec}, η and E_b as functions of *x* are plotted in the Fig.6(f). The BFST ceramic exhibits a relatively low dielectric breakdown strength (E_b) of 140 kV/cm. With the addition of BTO, E_b increases significantly, reaching a peak value of 420 kV/cm at x = 0.04. Meanwhile, the recoverable energy storage density

(W_{rec}) of the ceramics is also enhanced, with the highest value of 3.38 J/cm³ achieved at x = 0.08 in this work. However, the energy storage efficiency of the present ceramic remains relatively low due to large hysteresis of P-E curves, which calls for further systematic research to address this limitation. Fig. 6(g) depicts the Weibull distribution plots of the BFST-0.04BTO and BFST-0.08BTO ceramics. The corresponding Weibull moduli are calculated to be 21.17 and 13.63, respectively. These Weibull moduli suggest data reliability, and the characteristic breakdown field strengths are 415.71 kV/cm and 400.06 kV/cm, respectively.

Besides grain size, the band gap width (E_g) also affects the E_b of ceramics[10]. Fig. 7(a) exhibits the UV–vis absorption spectra of BFST-xBTO ceramics. The E_g value of BFST-xBTO ceramics was calculated based on the Tauc equation, as shown in Fig. 7(b)[41]. The E_g of the BFST-xBTO ceramics is presented in Fig. 7c. With the addition of BTO, the E_g of the ceramic is generally enhanced with some fluctuations, it is manifested as increasing first and then decreasing, with the highest value of 2.05 eV achieved at x = 0.04. A larger band gap requires more energy for electrons to move from the valence band to the conduction band, allowing the material to endure higher electric fields[42, 43]. Therefore, the large band gap plays a crucial role in enhancing the breakdown strength. The E_g value reaches its maximum at x=0.04, resulting in a higher E_b compared to the other compositions. The band gap changes might correlate with grain size in BFST-xBTO ceramics. BTO doping inhibits grain growth of BFST ceramics, which reduces the average grain size and increases the volume fraction of grain boundaries. Grain boundaries usually contain abundant oxygen vacancies, lattice distortions and defect states. These microstructural features can modify the electronic band structure and thus tune the optical band gap.

Figs. 8(a)-(e) show the high-temperature impedance spectra of BFST-xBTO ceramics. All the Z'–Z'' curves can be fitted using two cascaded R || CPE equivalent circuits. As seen, all Z' - Z'' curves exhibit an approximate semicircle, indicating that grain boundaries dominate the conduction process[44]. The results demonstrate that BTO doping contributes to an increase in impedance, indicating a significant enhancement

in the insulation properties of the ceramics. The observed impedance increase in BTO-modified BFST ceramics may be associated with both the high-resistivity BTO constituent and grain refinement. The activation energy (E_a) for grain boundary conductivity is calculated using the Arrhenius equation, as shown in Fig. 8(f). The E_a increases with the incorporation of BTO and lies between 0.78 eV and 1.16 eV, which is typical value for oxygen vacancy.

Figs. 9(a)-(e) show the O 1s XPS data of BFST-*x*BTO ceramics. The peak at ~528 eV (lower binding energy) corresponds to lattice oxygen, whereas the peak at ~530 eV (higher binding energy) is attributed to the influence of oxygen vacancies on the binding energies of neighboring oxygen atoms. Upon the incorporation of BTO, the relative area of the ~530 eV peak rises from 46.23% (x=0) to 58.83% (x=0.04) and subsequently decreases to 53.23% (x=0.08). These XPS findings demonstrate that BTO doping enhances the oxygen vacancy concentration. By combining impedance spectroscopy results with XPS analyses, it is inferred that oxygen vacancies are enriched near grain boundaries instead of inside grains. In addition, the SEM observations demonstrate an increase in the grain boundary density, which consequently gives rise to a higher concentration of oxygen vacancies within the grain boundary regions. The conduction mechanism of BFST-*x*BTO ceramics originates from localized oxygen vacancy hopping near grain boundaries, while grains with high unit cell symmetry and a large E_g prevent the long-range migration of oxygen vacancies across the ceramics - this accounts for the decreased dielectric loss and improved E_b.

4 Conclusions

BFST-*x*BTO ceramics were successfully synthesized through a conventional solid state reaction method. The BTO completely dissolves into perovskite lattice for the investigated composition of x = 0.02 - 0.08. BTO doping can effectively refine the grain size, concentrating more oxygen vacancy near the grain boundary while enhance the unit cell symmetry and band gap. As a result, dielectric loss decreases and dielectric break down strength increase to 420 kV/cm at x=0.04. Due to enhancement of E_b, the W_{rec} value reaches 3.38 J/cm^3 at x=0.08. Our results confirm that BTO doping is an

efficient approach to enhance the dielectric breakdown strength and energy storage capabilities of BFST ceramics, a strategy that might be extended to other Bi-based perovskite materials. Lead-free dielectric ceramics with high breakdown strength are urgently demanded for advanced energy storage capacitors. This BFST-*x*BTO ceramic system provides a feasible candidate for high-performance pulsed power capacitors.

Acknowledgments

This work was supported by the National Natural Science Foundation of China under Grants No. 52172004, and by the Jilin Provincial Science and Technology Development Project under Grant No. 20230402069GH.

References

[1] Agajie T F, Ali A, Fopah-Lele A, et al. A Comprehensive Review on Techno-Economic Analysis and Optimal Sizing of Hybrid Renewable Energy Sources with Energy Storage Systems [J]. Energies, 2023, 16(2).

[2] Hao X. A review on the dielectric materials for high energy-storage application [J]. Journal of Advanced Dielectrics, 2013, 03(01).

[3] Kousksou T, Bruel P, Jamil A, et al. Energy storage: Applications and challenges [J]. Solar Energy Materials and Solar Cells, 2014, 120: 59-80.

[4] Zhang Y, He X, Cong X, et al. Enhanced energy storage performance of polyethersulfone-based dielectric composite via regulating heat treatment and filling phase [J]. Journal of Alloys and Compounds, 2023, 960.

[5] Adediji Y B, Adeyinka A M, Yahya D I, et al. A review of energy storage applications of lead-free BaTiO3-based dielectric ceramic capacitors [J]. Energy, Ecology and Environment, 2023, 8(5): 401-419.

[6] Liu X, Yang T, Shen B, et al. Enhancing the Energy Storage Performance in Lead-Based Antiferroelectric Ceramics via Pb(Zr0.88Sn0.12)O3/(Pb0.875La0.05Sr0.05)(Zr0.695Ti0.005Sn0.3)O3-Derived Laminated Composite Structures [J]. ACS Applied Energy Materials, 2023, 6(3): 1218-1227.

[7] Xun B, Song A, Yu J, et al. Lead-Free BiFeO3-BaTiO3 Ceramics with High Curie

Temperature: Fine Compositional Tuning across the Phase Boundary for High Piezoelectric Charge and Strain Coefficients [J]. ACS Applied Materials & Interfaces, 2021, 13(3): 4192-4202.

[8] Bell A J, Deubzer O. Lead-free piezoelectrics—The environmental and regulatory issues [J]. MRS Bulletin, 2018, 43(8): 581-587.

[9] Pattipaka S, Lim Y, Son Y H, et al. Ceramic-Based Dielectric Materials for Energy Storage Capacitor Applications [J]. Materials, 2024, 17(10).

[10] Yang Z, Du H, Jin L, et al. High-performance lead-free bulk ceramics for electrical energy storage applications: design strategies and challenges [J]. Journal of Materials Chemistry A, 2021, 9(34): 18026-18085.

[11] Qi H, Xie A, Zuo R. Local structure engineered lead-free ferroic dielectrics for superior energy-storage capacitors: A review [J]. Energy Storage Materials, 2022, 45: 541-567.

[12] Deka B, Cho K-H. BiFeO3-Based Relaxor Ferroelectrics for Energy Storage: Progress and Prospects [J]. Materials, 2021, 14(23).

[13] Ravindran P, Vidya R, Kjekshus A, et al. Theoretical investigation of magnetoelectric behavior inBiFeO3 [J]. Physical Review B, 2006, 74(22).

[14] Li L, Liu H, Wen G, et al. Structural evolution and dielectric response of (1-x)BiFeO3-xSrTiO3 ceramics [J]. Ceramics International, 2018, 44: S69-S71.

[15] Chang C-J, Qi X. Dielectric relaxation and high recoverable energy density in (1-x)(0.3BiFeO3-0.7SrTiO3)-xK0.5Na0.5NbO3 ceramics [J]. Ceramics International, 2022, 48(17): 25610-25620.

[16] Ghosh T K, Khan M K R, Rahman M M, et al. Enhanced electrical, optical and magnetic properties of BiFeO3 perovskite nanoparticles co-doped with Y and Cu [J]. AIP Advances, 2024, 14(4).

[17] Preethi A J, Ragam M. Effect of doping in multiferroic BFO: A review [J]. Journal of Advanced Dielectrics, 2021, 11(06).

[18] Jan A, Liu H, Hao H, et al. Lead-free relaxor-ferroelectric ceramics for high-energy-storage applications [J]. Journal of Materials Chemistry C, 2020, 8(26): 8962-

8970.

[19] Wang Z, Cao M, Yao Z, et al. Giant permittivity and low dielectric loss of SrTiO3 ceramics sintered in nitrogen atmosphere [J]. Journal of the European Ceramic Society, 2014, 34(7): 1755-1760.

[20] Correia T M, McMillen M, Rokosz M K, et al. A Lead-Free and High-Energy Density Ceramic for Energy Storage Applications [J]. Journal of the American Ceramic Society, 2013, 96(9): 2699-2702.

[21] Esquivel-Elizondo J R, Hinojosa B B, Nino J C. Bi2Ti2O7: It Is Not What You Have Read [J]. Chemistry of Materials, 2011, 23(22): 4965-4974.

[22] Hector A L, Wiggin S B. Synthesis and structural study of stoichiometric Bi2Ti2O7 pyrochlore [J]. Journal of Solid State Chemistry, 2004, 177(1): 139-145.

[23] Yan F, Bai H, Ge G, et al. Composition and Structure Optimized BiFeO3-SrTiO3 Lead-Free Ceramics with Ultrahigh Energy Storage Performance [J]. Small, 2022, 18(10).

[24] Fan Q, Zhou C, Zeng W, et al. Normal-to-relaxor ferroelectric phase transition and electrical properties in Nb-modified 0.72BiFeO3-0.28BaTiO3 ceramics [J]. Journal of Electroceramics, 2015, 36(1-4): 1-7.

[25] Song Y, Shen Y, Liu H, et al. Improving the dielectric constants and breakdown strength of polymer composites: effects of the shape of the BaTiO3 nanoinclusions, surface modification and polymer matrix [J]. Journal of Materials Chemistry, 2012, 22(32).

[26] Zhao Y, Yang B, Liu Y, et al. Capturing Carriers and Driving Depolarization by Defect Engineering for Dielectric Energy Storage [J]. ACS Applied Materials & Interfaces, 2022, 14(5): 6547-6559.

[27] Wu C, Qiu X, Ge W, et al. A co-doping strategy to achieve high energy storage performance in BiFeO3-based ceramics [J]. Ceramics International, 2023, 49(17): 29218-29228.

[28] Zhao P, Fang Z, Zhang X, et al. Aliovalent Doping Engineering for A- and B-Sites

with Multiple Regulatory Mechanisms: A Strategy to Improve Energy Storage Properties of Sr0.7Bi0.2TiO3-Based Lead-Free Relaxor Ferroelectric Ceramics [J]. ACS Applied Materials & Interfaces, 2021, 13(21): 24833-24855.

[29] Su W-F, Lu Y-T. Synthesis, phase transformation and dielectric properties of sol–gel derived Bi2Ti2O7 ceramics [J]. Materials Chemistry and Physics, 2003, 80(3): 632-637.

[30] Khanal G P, Fujii I, Ueno S, et al. Phase evolution and <110> - orientation mechanism in RTGG - processed BaTiO3 ceramics with electrical properties [J]. Journal of the American Ceramic Society, 2021, 104(9): 4649-4658.

[31] Nicola A. Spaldin R S. History of Ferroelectrics -- A Crystallography Perspective [J]. IUCr Newsletter, 2021.

[32] Liang X, Wang J, Hu W. Atomic scale octahedral distortion and enhanced collective polarity underlying large polarization in ferroelectric perovskite oxides [J]. Journal of Materiomics, 2026, 12(2).

[33] Luo C, Feng Q, Luo N, et al. Effect of Ca2+/Hf4+ modification at A/B sites on energy-storage density of Bi0.47Na0.47Ba0.06TiO3 ceramics [J]. Chemical Engineering Journal, 2021, 420.

[34] Wu C, Qiu X, Liu C, et al. Enhanced Relaxor Behavior and Energy - Storage Properties in Na0.5Bi0.5TiO3 - Based Ceramics by Doping the Complex Ions (Al0.5Nb0.5)4+ [J]. physica status solidi (a), 2022, 219(5).

[35] Wang D, Wang G, Murakami S, et al. BiFeO3-BaTiO3: A new generation of lead-free electroceramics [J]. Journal of Advanced Dielectrics, 2019, 08(06).

[36] Zhu C, Zhao Q, Cai Z, et al. High reliable non-reducible ultra-fine BaTiO3-based ceramics fabricated via solid-state method [J]. Journal of Alloys and Compounds, 2020, 829.

[37] Gui D-Y, Ma X-Y, Yuan H-D, et al. Mn- and Yb-Doped BaTiO3-(Na0.5Bi0.5)TiO3 Ferroelectric Relaxor with Low Dielectric Loss [J]. Materials, 2023, 16(6).

[38] Cai L, Pattnaik R, Lundeen J, et al. Piezoelectric polar nanoregions and relaxation-

coupled resonances in relaxor ferroelectrics [J]. Physical Review B, 2018, 98(13).

[39] Chakraborty M, Rai V K, Mitra K. Investigation on the electrical and optical properties of some zinc titanate ceramics [J]. Pramana, 2019, 92(3).

[40] Zhou X X, Tang Y C, Li H Z, et al. BiAlO3 - modified BiFeO3–BaTiO3 high Curie temperature lead - free piezoelectric ceramics with enhanced performance [J]. Rare Metals, 2023, 42(11): 3839-3850.

[41] Kapuri S, Mukhopadhyay L, Rai V K. Negative thermal quenching effect in Er3+/Yb3+: Ca2ZnWO6 phosphors: Towards optical thermometry and anti-counterfeiting applications [J]. Materials Research Bulletin, 2026, 193.

[42] Li T, Jiang X, Li J, et al. Ultrahigh Energy-Storage Performances in Lead-free Na0.5Bi0.5TiO3-Based Relaxor Antiferroelectric Ceramics through a Synergistic Design Strategy [J]. ACS Applied Materials & Interfaces, 2022, 14(19): 22263-22269.

[43] Qi H, Xie A, Tian A, et al. Superior Energy - Storage Capacitors with Simultaneously Giant Energy Density and Efficiency Using Nanodomain Engineered BiFeO3 - BaTiO3 - NaNbO3 Lead - Free Bulk Ferroelectrics [J]. Advanced Energy Materials, 2019, 10(6).

[44] Kindelmann M, Povstugar I, Kuffer S, et al. Controlling Grain Boundary Segregation to Tune the Conductivity of Ceramic Proton Conductors [J]. Advanced Energy Materials, 2024, 15(9).

Figure captions

Fig. 1. XRD patterns of the BFST-*x*BTO ceramics: (a) 2θ = 10–80°, (b)-(d) magnified diffraction peaks corresponding to the (110), (111), and (200) crystal planes.

Fig. 2. Rietveld-refined XRD data of the BFST-*x*BTO ceramics: (a) $x = 0$, (b) $x = 0.02$, (c) $x = 0.04$, (d) $x = 0.06$, and (e) $x = 0.08$; (f) Unit cell parameters and unit cell volume of the BFST-*x*BTO ceramics as a function of x.

Table 1. The atomic position table of BFST-*x*BTO

Fig. 3. SEM micrographs (a–e) and grain size distribution histograms (insets of (a)–(e)) of the BFST-*x*BTO ceramics; (f) Average grain size as a function of BTO content.

Fig. 4. (a) SEM micrographs and (b)-(f) corresponding energy-dispersive x-ray spectroscopy (EDS) elemental mapping analysis of the BFST-0.04BTO ceramics.

Fig. 5. (a)-(e) The ε_r-T curves and the tanδ-T curves of BFST-*x*BTO ceramics; (f) The ε_r-T (solid lines) curves and the tanδ-T (dash lines) curves at l MHz.

Fig. 6. The *P-E* loops of BFST-*x*BTO ceramics before breakdown: (a) $x = 0$, (b) $x = 0.02$, (c) $x = 0.04$, (d) $x = 0.06$, (e) $x = 0.08$. (f) The W_{rec}, η and E_b corresponding to the BFST-*x*BTO ceramics. (g) Weibull distribution of breakdown strength for BFST-0.04BTO and BFST-0.08BTO ceramics.

Fig. 7. (a) The UV-vis absorption spectra of BFST-*x*BTO ceramics. (b) The calculated E_g values by using the Tauc equation. (c) The E_g as a function of x for the BFST-*x*BTO ceramics.

Fig. 8. The impedance spectra of BFST-*x*BTO ceramics: (a) $x = 0$, (b) $x = 0.02$, (c) $x = 0.04$, (d) $x = 0.06$ and (e) $x = 0.08$. (f) The activation energy (E_a) calculated by the Arrhenius equation.

Fig. 9. XPS survey spectra of the BFST-*x*BTO ceramics: (a) $x = 0$, (b) $x = 0.02$, (c) $x = 0.04$, (d) $x = 0.06$, and (e) $x = 0.08$.

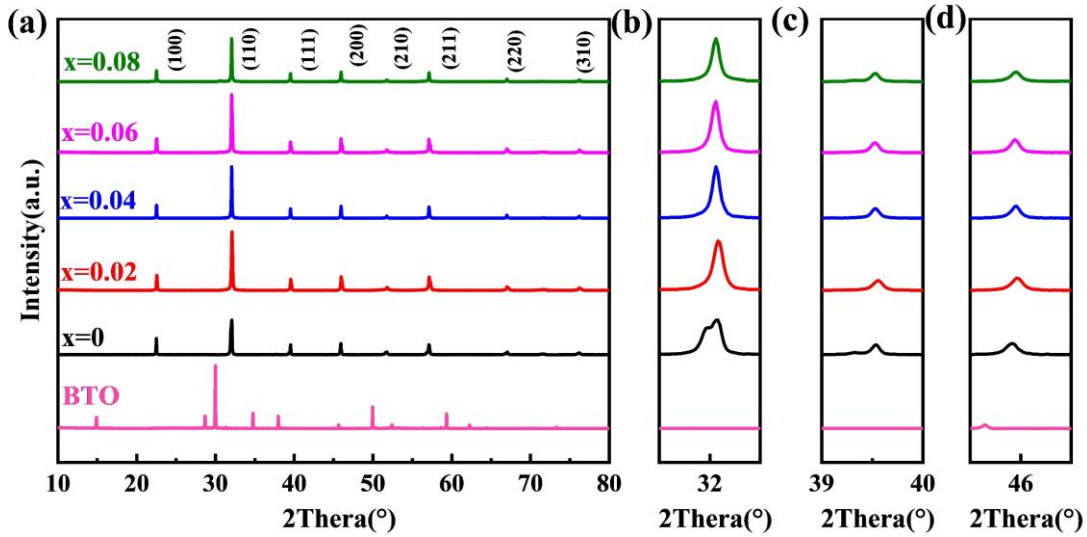


Fig. 1. XRD patterns of the BFST-*x*BTO ceramics: (a) 2θ = 10–80°, (b)-(d) magnified diffraction peaks corresponding to the (110), (111), and (200) crystal planes.

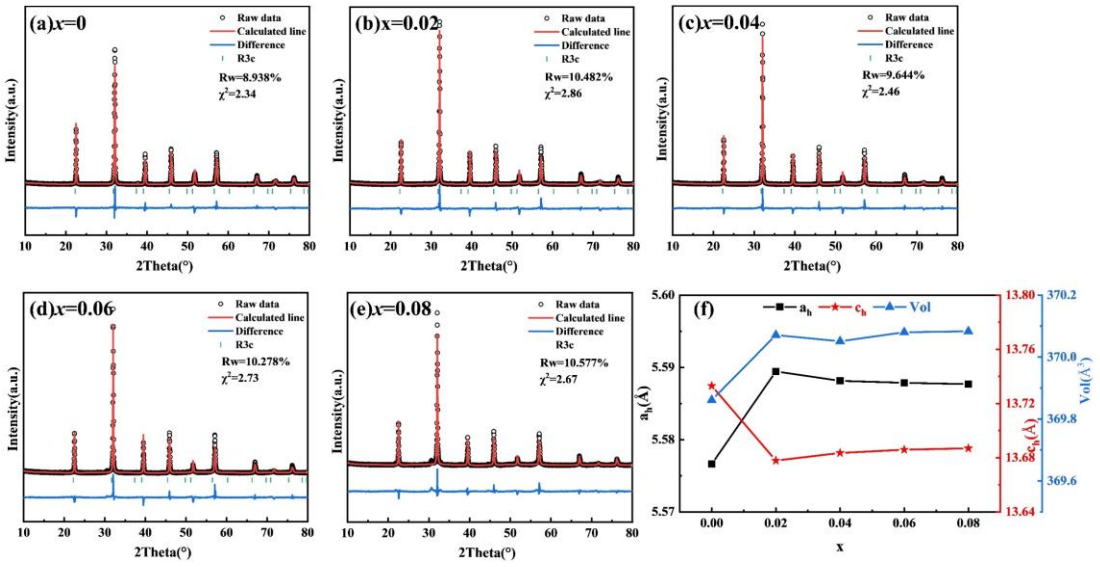


Fig. 2. Rietveld-refined XRD data of the BFST-*x*BTO ceramics: (a) $x = 0$, (b) $x = 0.02$, (c) $x = 0.04$, (d) $x = 0.06$, and (e) $x = 0.08$; (f) Unit cell parameters and unit cell volume of the BFST-*x*BTO ceramics as a function of x.

Table 1

The atomic position table of BFST-xBTO

Atom	**Parameter**	**x=0**	**x=0.02**	**x=0.04**	**x=0.06**	**x=0.08**
Bi	x	0	0	0	0	0
	y	0	0	0	0	0
	z	0.219	0.235	0.236	0.235	0.234
Sr	x	0	0	0	0	0
	y	0	0	0	0	0
	z	0.219	0.235	0.236	0.235	0.234
Fe	x	0	0	0	0	0
	y	0	0	0	0	0
	z	0.99	0.96	0.97	0.97	0.96
Ti	x	0	0	0	0	0
	y	0	0	0	0	0
	z	0.99	0.96	0.97	0.97	0.96
O	x	0.107	0.132	0.184	0.155	0.150
	y	0.326	0.314	0.316	0.331	0.349
	z	0.083	0.067	0.063	0.072	0.074

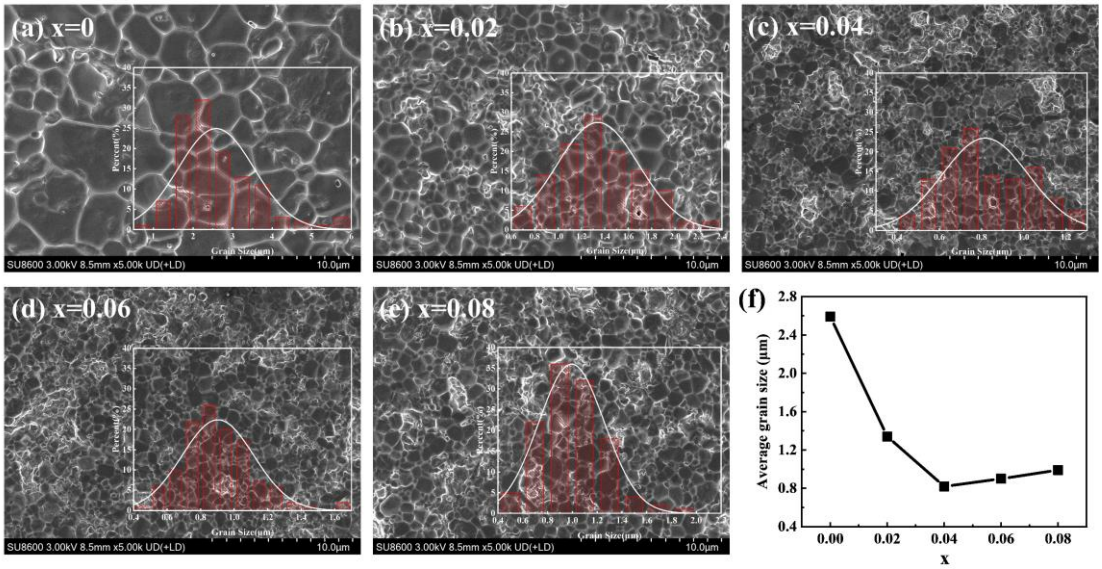


Fig. 3. SEM micrographs (a–e) and grain size distribution histograms (insets of (a)–(e)) of the BFST-*x*BTO ceramics; (f) Average grain size as a function of BTO content.

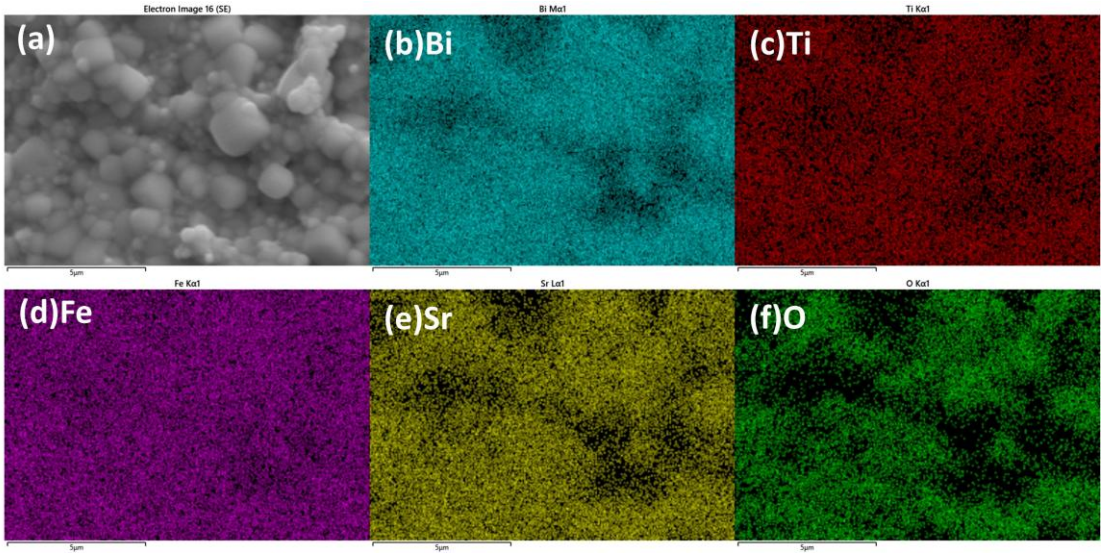


Fig. 4. (a) SEM micrographs and (b)-(f) corresponding energy-dispersive x-ray spectroscopy (EDS) elemental mapping analysis of the BFST-0.04BTO ceramics.

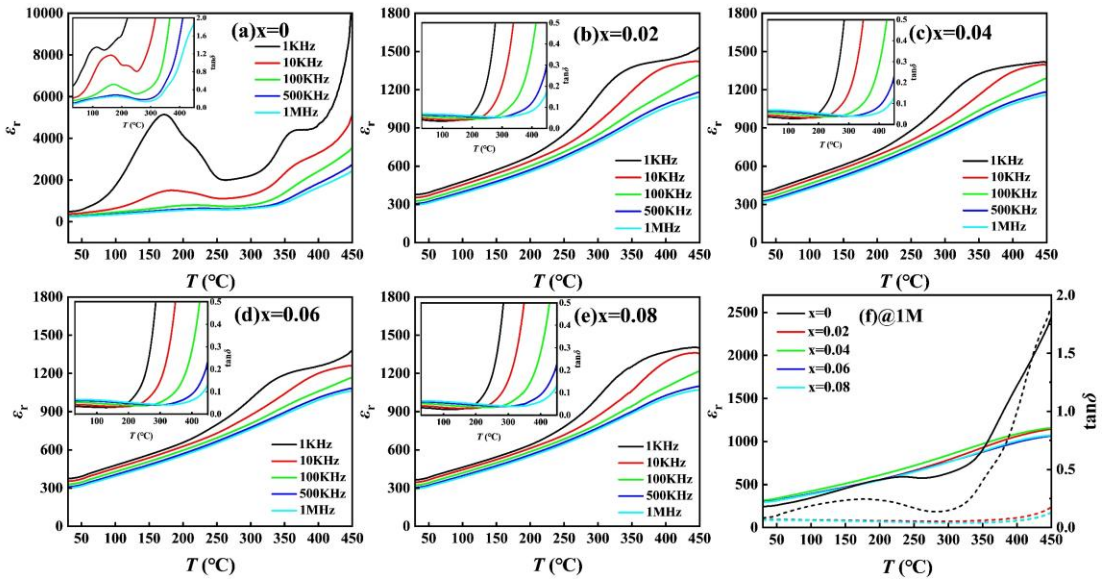


Fig. 5. (a)-(e) The ε_r-T curves and the tanδ-T curves of BFST-*x*BTO ceramics; (f) The ε_r-T (solid lines) curves and the tanδ-T (dash lines) curves at l MHz.

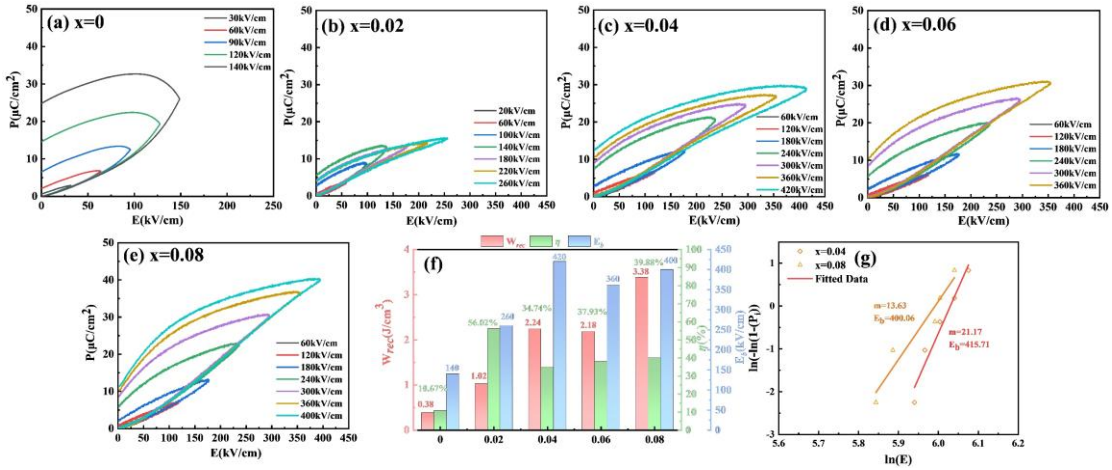


Fig. 6. The *P-E* loops of BFST-*x*BTO ceramics before breakdown: (a) $x = 0$, (b) $x = 0.02$, (c) $x = 0.04$, (d) $x = 0.06$, (e) $x = 0.08$. (f) The W_{rec} , η and E_b corresponding to the BFST-*x*BTO ceramics. (g) Weibull distribution of breakdown strength for BFST-0.04BTO and BFST-0.08BTO ceramics.

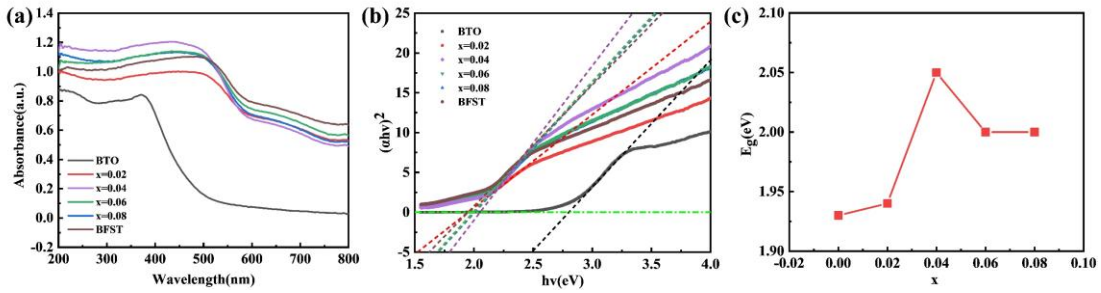


Fig. 7. (a) The UV-vis absorption spectra of BFST-*x*BTO ceramics. (b) The calculated E_g values by using the Tauc equation. (c) The E_g as a function of *x* for the BFST-*x*BTO ceramics.

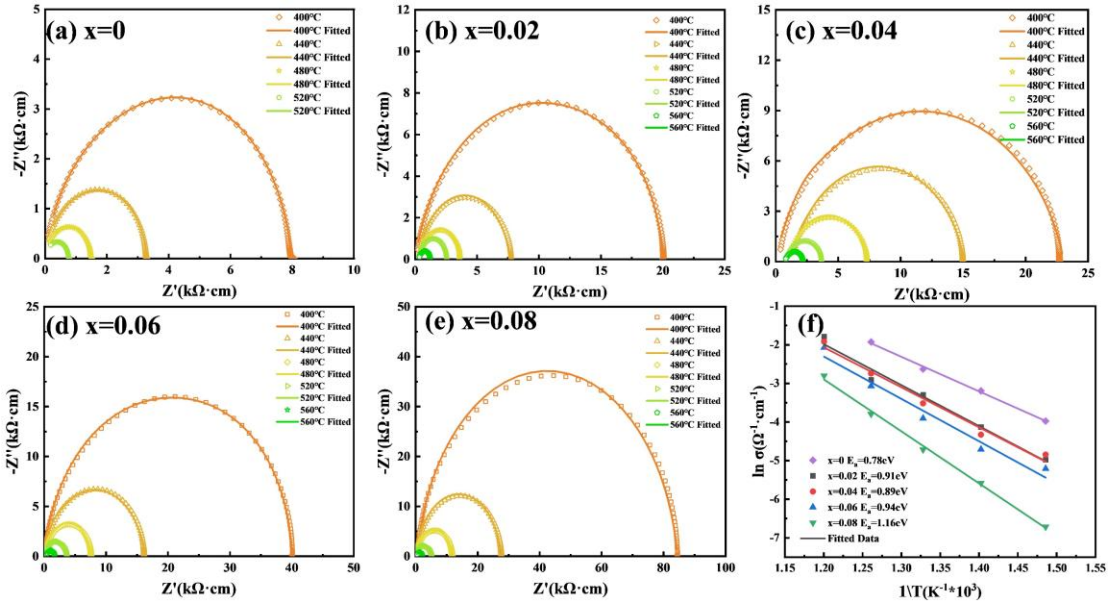


Fig. 8. The Z' - Z'' curves of BFST-xBTO ceramics: (a) x = 0, (b) x = 0.02, (c) x = 0.04, (d) x = 0.06 and (e) x = 0.08. (f) The activation energy (E_a) calculated by the Arrhenius equation.

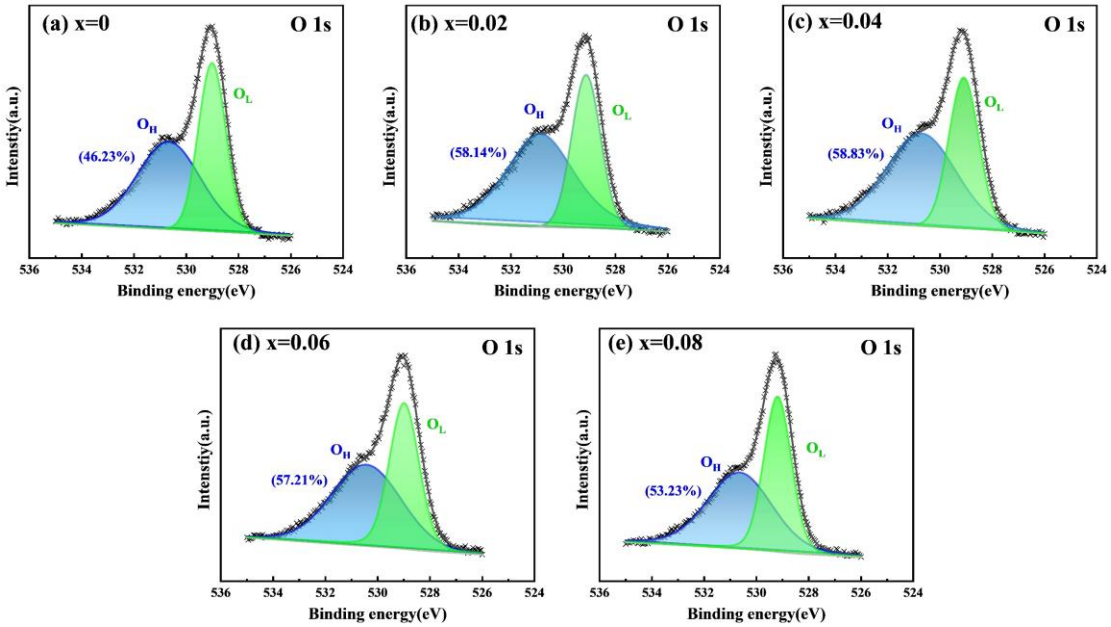


Fig. 9. XPS survey spectra of the BFST-*x*BTO ceramics: (a) $x = 0$, (b) $x = 0.02$, (c) $x = 0.04$, (d) $x = 0.06$, and (e) $x = 0.08$.